
PocketSR: The Super-Resolution Expert in Your Pocket Mobiles

Haoze Sun*, Linfeng Jiang*, Fan Li, Renjing Pei, Zhixin Wang, Yong Guo, Jiaqi Xu, Haoyu Chen, Jin Han, Fenglong Song, Yujiu Yang[✉], Wenbo Li[✉]

Tsinghua University Joy Future Academy HKUST (GZ)

shz22@tsinghua.org.cn yang.yujiu@sz.tsinghua.edu.cn fenglinglb@gmail.com

Abstract

Real-world image super-resolution (RealSR) aims to enhance the visual quality of in-the-wild images, such as those captured by mobile phones. While existing methods leveraging large generative models demonstrate impressive results, the high computational cost and latency make them impractical for edge deployment. In this paper, we introduce PocketSR, an ultra-lightweight, single-step model that brings generative modeling capabilities to RealSR while maintaining high fidelity. To achieve this, we design LiteED, a highly efficient alternative to the original computationally intensive VAE in SD, reducing parameters by 97.5% while preserving high-quality encoding and decoding. Additionally, we propose online annealing pruning for the U-Net, which progressively shifts generative priors from heavy modules to lightweight counterparts, ensuring effective knowledge transfer and further optimizing efficiency. To mitigate the loss of prior knowledge during pruning, we incorporate a multi-layer feature distillation loss. Through an in-depth analysis of each design component, we provide valuable insights for future research. PocketSR, with a model size of 146M parameters, processes 4K images in just 0.8 seconds, achieving a remarkable speedup over previous methods. Notably, it delivers performance on par with state-of-the-art single-step and even multi-step RealSR models, making it a highly practical solution for edge-device applications.

1 Introduction

Real-world image super-resolution (RealSR) [1–6] is a fundamental task in computer vision that reconstructs high-quality images from low-quality inputs. With applications spanning smartphone photography, medical imaging, and remote sensing, RealSR has driven extensive research interest and development. Recent breakthroughs in generative modeling—particularly diffusion models [7–11]—have opened new frontiers in SR by leveraging powerful generative priors to recover intricate textures and realistic structures, significantly enhancing image quality.

Scaling up text-to-image (T2I) diffusion models (*e.g.*, from SD1.5 [9] to SD3 [12] or FLUX [13]) has been shown to markedly improve SR performance [14]. Additionally, integrating multimodal large language models to generate detailed and accurate image descriptions further unlocks these models’ generative potential [15–17]. However, the substantial computational cost and slow inference speed of such large-scale models limit their practical deployment. Consequently, research efforts have shifted toward efficient SR diffusion methods, focusing on lightweight architectures [18] and reduced sampling steps [19–23]. Yet, deploying these models on resource-constrained edge devices remains a formidable challenge.

Given that low-resolution (LR) inputs provide a rich and detailed prior—far more informative than the sparse textual cues in T2I generation—it is possible to achieve competitive SR performance with

*Equal Contribution ✉ Corresponding Author

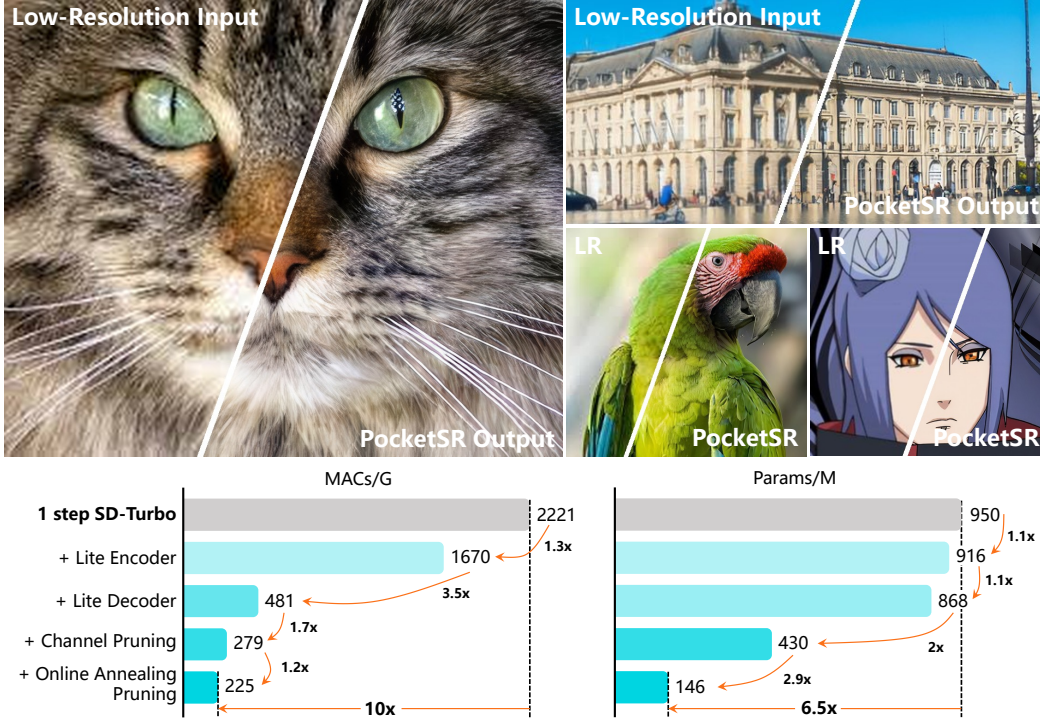


Figure 1: Visualization of the real-world image super-resolution results and efficiency of our proposed method. To enable the practical application of diffusion-based SR models, we introduce PocketSR, an ultra-lightweight, single-step solution. The top visual examples demonstrate that PocketSR achieves high-quality super-resolution across diverse scenes, preserving fine details and textures. Best viewed zoomed in. The bottom section highlights the significant reduction in parameters (10 \times) and computational cost (6.5 \times), allowing our model to process 4K images in just 0.8 seconds—dramatically outpacing existing methods.

a significantly compressed model. Motivated by this insight, we conduct a thorough analysis of the core components of diffusion models, including the variational autoencoder (VAE) and the U-Net architecture, and propose tailored strategies to maintain high-fidelity and realistic generation while substantially reducing the model size. Our approach is built upon three key innovations:

Lite Encoder & Decoder (LiteED). We introduce a highly compressed encoder-decoder design featuring an ultra-compact encoder for efficient LR feature extraction and conditioning, coupled with a tiny decoder for high-quality reconstruction. To mitigate potential losses in representational capacity, we incorporate a Dual-Path Feature Injection mechanism that enriches U-Net inputs with additional high-dimensional feature channels and Adaptive Skip Connections that retain critical information. The resulting LiteAE contains only 2M parameters, drastically improving model efficiency while preserving image quality.

Online Annealing Pruning for U-Net. Recognizing the extensive generative priors embedded within U-Net architectures, we go beyond straightforward channel pruning [18] by introducing an online annealing pruning strategy. In this approach, lightweight modules are gradually integrated alongside existing components (*e.g.*, residual blocks, self-attention layers, and feed-forward networks), while the contributions of original modules are progressively annealed to zero. This smooth transition ensures a stable knowledge transfer to the pruned architecture. Additionally, we conduct a comprehensive ablation study to determine optimal pruning positions, ensuring that our lightweight model retains strong generative capabilities.

Multi-layer Feature Distillation. Prior studies [18, 24] have demonstrated that feature-space distillation offers a more stable optimization process compared to distillation in the image domain. Motivated by this observation, we adopt a multi-layer, multi-scale distillation scheme to facilitate more reliable knowledge transfer. When combined with our online annealing pruning strategy, this approach substantially reduces computational cost while effectively preserving generative priors.

Through these architectural optimizations, we further integrate adversarial training to develop PocketSR, an ultra-lightweight, one-step diffusion-based SR model with only 146M parameters—just 10.4% of the size of StableSR [3] and 8.2% of OSEDiff [22]. Despite its compactness, PocketSR achieves performance on par with state-of-the-art approaches while significantly reducing computational complexity and inference time, as illustrated in Sect. 4.2. Notably, it processes a 4K image in just 0.8 seconds—7 times faster than OSEDiff [22]. Our findings demonstrate that with carefully designed modifications, diffusion-based SR models can be both lightweight and powerful, paving the way for practical deployment in real-world applications.

2 Related Work

2.1 Real-world Image Super-Resolution

Real-world image super-resolution (SR) aims to recover realistic details from degraded inputs while maintaining overall fidelity. Early image super-resolution (ISR) methods [25–28] often converge to the statistical mean of plausible solutions, resulting in overly smoothed outputs and loss of fine details in real-world scenarios. To overcome this, several works [29, 2, 1, 30–32] have explored generative adversarial networks (GANs) for texture enhancement. However, due to inherent limitations such as mode collapse and training instability [33, 34], GAN-based methods still struggle to produce realistic textures. More recently, diffusion models [7–11] have shown strong generative capabilities in synthesizing fine-grained details and realistic textures, making them a promising alternative for real-world SR.

2.2 Diffusion-based ISR

Recent advances in diffusion models, especially in text-to-image (T2I) synthesis (e.g., SD3 [12], FLUX [13]), have led to the development of pre-trained diffusion-based SR methods such as StableSR [3], DiffBIR [4], PASD [5], CoSeR [35], SeeSR [16], and SUPIR [15]. These approaches benefit from the strong image priors of T2I models, achieving impressive results. However, their reliance on multi-step inference introduces high latency and substantial computational cost.

To address this, recent works aim to reduce inference time by distilling multi-step models into one- or few-step variants. ResShift [6] accelerates inference by learning residual transitions from LR to HR images via a Markov chain. Building on this, Wang et al. [19] condense multi-step capabilities into single-step networks. OSEDiff [22] further leverages VSD [36] to incorporate T2I knowledge efficiently. Despite these advances, single-step SR methods still remain computationally heavier than traditional GAN-based models, limiting their deployment on edge devices and highlighting the need for better efficiency–quality trade-offs.

2.3 Efficient Diffusion Models

Recent efforts on efficient diffusion models [37–42, 24] focus on architectural optimization to reduce redundancy in large-scale models. SnapFusion [42] disentangles the contributions of individual modules to balance efficiency and accuracy. MobileDiff [40] improves efficiency by relocating Transformer blocks to lower-resolution stages. SnapGen [24] cuts computation and model size by removing high-resolution attention and replacing standard convolutions with depthwise separable ones. AdcSR [18] further explores one-step SR model efficiency. In Sect. 4.3, we compare our design with AdcSR and show that our approach achieves better performance with higher compression.

3 Method

Our PocketSR framework, utilizing SD-Turbo² as the backbone, achieves extreme model compression through a two-stage training pipeline. In the first stage, we replace the original Stable Diffusion’s (SD) variational autoencoder with the Lite Encoder-Decoder (LiteED), with all parameters set to be trainable. In the second stage, we freeze LiteED and apply our pruning strategies to the U-Net, gradually removing redundant components.

²<https://huggingface.co/stabilityai/sd-turbo>

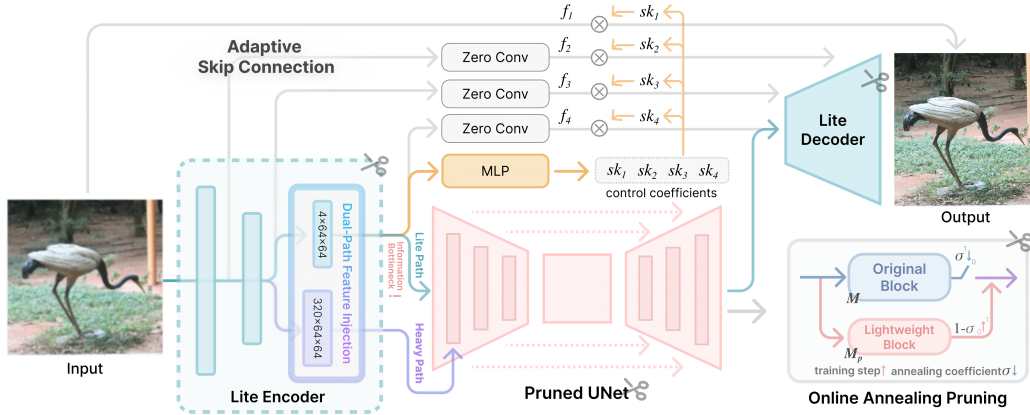


Figure 2: Overview of PocketSR framework. We replace the original Stable Diffusion variational autoencoder with LiteED, and apply online annealing pruning and multi-layer feature distillation strategies to the diffusion U-Net, effectively reducing model parameters and computational complexity while maintaining excellent super-resolution performance.

3.1 Lite Encoder & Decoder

We propose LiteED, an ultra-lightweight encoder-decoder architecture designed for edge-side super-resolution. To reduce complexity, we simplify the SD encoder to several convolutional layers, while maintaining effective feature extraction. Additionally, we replace the original decoder with a lightweight alternative that offers substantial improvements in efficiency while preserving comparable image fidelity (detailed in the supplementary materials). Notably, the decoder in LiteED is modular and can be substituted with a more powerful variant to enhance reconstruction quality, albeit at the cost of efficiency. The decoder is initialized from an open-source model³, while the encoder is randomly initialized.

To supplement the ultra-light encoder and enrich the representational capacity, we propose an adaptive skip connection mechanism in LiteED, as depicted in Figure 2. Specifically, four control coefficients are generated from the encoder output via an MLP to modulate the multi-scale skip connections. This adaptive mechanism allows the model to selectively integrate input features during decoding, effectively mitigating the loss of information due to encoder compression. Additionally, to stabilize training, we incorporate zero-convolution into the skip connections.

Dual-path Feature Injection. We identify an information bottleneck between the original SD encoder and the U-Net. For a 512×512 image, the output feature size of the SD encoder’s last ResBlock is $[N, 512, 64, 64]$, but it is compressed to $[N, 4, 64, 64]$ in the final convolutional layer. This $128\times$ reduction in feature dimensionality may lead to substantial information loss, negatively impacting super-resolution performance. To address this issue and improve the fidelity of the result, we propose a dual-path feature injection mechanism. Specifically, in our encoder, an additional high-dimensional feature of size $[N, 320, 64, 64]$ is extracted after the second convolutional layer of LiteAE and injected into the U-Net following the initial block. This strategy enhances the information flow, allowing for more robust feature extraction. As for feature injection, we employ cross normalization [43], which has been shown to facilitate fast and stable convergence.

Despite its lightweight design, LiteED proves to be more effective in practice than networks with several times higher computational complexity. Moreover, the decoder in LiteED can be replaced with a larger-capacity network, which leads to better performance as demonstrated in our experiments.

3.2 U-Net Pruning

3.2.1 Online Annealing Pruning

Pruning is a straight-forward and effective model compression technique, which is widely used in efficient image generation [38, 41, 40, 42, 24]. In this paper, we propose online annealing pruning, a

³<https://github.com/madebyollin/taesd>

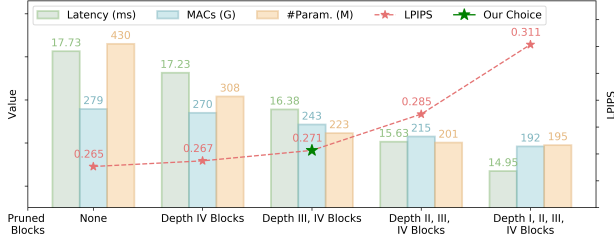


Figure 3: Analysis of the impact of pruning residual blocks at different depths using the widely adopted RealSR [44] test set, measured by the LPIPS [45] metric. The inference resolution is 512×512 , and we report the maximum inference speed on a single GPU with about 19.5 TFLOPS for FP32.

Table 1: Comparison of the computational efficiency of the SD network and its modules before and after our streamlining. We highlight the computational efficiency of the original SD and the improvements brought by PocketSR.

Network	Computational Efficiency		
	Time (ms)	MACs (G)	#Param. (M)
Lite Encoder	↓99% 0.2	↓99% 8.1	↓98% 0.8
SD Encoder	22.6	559.5	34.2
Pruned U-Net	↓53% 12.5	↓64% 146.1	↓83% 144.2
SD U-Net	26.7	401.9	866
Lite Decoder	↓90% 3.0	↓94% 70.7	↓98% 1.2
SD Decoder	30.3	1259.7	49.4
PocketSR	↓80% 15.7	↓90% 224.9	↓85% 146.2
Original SD	79.7	2221.2	949.6

stable and efficient pruning strategy specifically designed for SR. Existing Diffusion U-Net pruning methods typically simply discard [40, 42] or replace pruned modules [41, 24], which leads to a significant loss of prior information. Our pruning strategy preserves the prior information through online knowledge transfer. As shown in Figure 2, we connect the original module M in parallel with a lightweight replacement module M_P . During the training process, we continuously increase the contribution of the lightweight module, while gradually annealing the contribution of the original module to zero:

$$\mathbf{y} = \sigma \cdot M(\mathbf{x}) + (1 - \sigma) \cdot M_P(\mathbf{x}), \quad (1)$$

where \mathbf{x} and \mathbf{y} represent the module input and output, respectively. The annealing coefficient is defined as $\sigma = \min(0, (T - t) / T)$, where T is the total number of annealing steps, and t denotes the current training step. The parameters of the original module are frozen during training. Once training is complete, the original module is replaced with the lightweight module. The pruned modules are permanently removed at inference time, yielding a highly compact and efficient model. Our experiments show that this online pruning approach can better preserve the diffusion prior and generate more realistic textures (see Sect. 4.3).

3.2.2 Pruning Implementation

Diffusion U-Net comprises four computationally expensive module types: residual blocks, cross-attention layers, self-attention layers, and feed-forward networks (FFNs). To reduce the number of parameters and computational cost while preserving performance, we replace each module with a carefully chosen lightweight counterpart. For residual blocks, we replace all convolutions with depthwise separable convolutions [46], significantly reducing the number of parameters. Since text input is entirely discarded, cross-attention layers are replaced with ultra-lightweight FFNs. Self-attention layers are approximated using linear attention to reduce computational cost. Finally, the hidden dimension of the FFN is reduced to one-fourth of its original size.

We also observe that the pruning location has a significant impact on model performance, with its effect varying according to the module’s depth within the network. Specifically, *shallower modules exert a greater influence on super-resolution quality, while deeper blocks can be pruned with minimal impact*. Taking SD’s U-Net as an example, we label the depths as {I, II, III, and IV}, from shallow to deep. Figure 3 illustrates the trade-off between performance and efficiency when pruning residual blocks at different depths. Our results show that pruning at deeper levels (III and IV) significantly reduces parameter count and computational cost while having negligible impact on performance. While pruning shallower modules yields greater efficiency gains, it leads to a more noticeable drop in final performance.

We interpret this phenomenon as deeper layers in the U-Net of a generative diffusion model primarily process high-level information [47, 48], such as layout and style, which contributes less to the SR task. This characteristic makes a free lunch for pruning. Our findings extend beyond residual blocks to other network modules, *e.g.*, self-attention, cross-attention, and FFNs, indicating a general pruning strategy for SR networks. Balancing efficiency and effectiveness, we prune residual blocks and FFNs at depths III and IV, while self-attention layers are pruned at depth IV. Additionally, we prune all cross-attention layers, as their impact on super-resolution quality is minimal. Detailed ablation experiments on all network module pruning locations are provided in the supplementary material.

3.2.3 Multi-layer Feature Distillation

To better preserve generative priors during pruning, we introduce a feature-level knowledge distillation strategy. Due to the architectural mismatch between the models before and after pruning, single-layer distillation may result in training instability. Instead, we adopt a multi-layer global distillation scheme to enhance robustness and enable stable knowledge transfer:

$$\mathcal{L}_{\text{distill}} = \mathbb{E} \left[\sum_l \left\| f_{\text{pre-pruning}}^l - \phi \left(f_{\text{post-pruning}}^l \right) \right\|_2^2 \right], \quad (2)$$

where $f_{\text{pre-pruning}}^l$ and $f_{\text{post-pruning}}^l$ denote the feature representations from the l -th layer of the models before and after pruning, respectively. The mapping function $\phi(\cdot)$ is implemented as a lightweight, trainable projection module composed of a single convolutional layer.

3.3 Training Details

Beyond the aforementioned lightweight optimizations, we further investigate the impact of channel reduction on model performance, which is compatible with our online annealing pruning strategy. Notably, direct channel reduction can substantially weaken the model’s learned priors. However, this adverse effect is markedly mitigated when integrated with the proposed multi-layer feature distillation strategy. Comprehensive experimental results are provided in the supplementary materials. To strike a balance between efficiency and performance, we reduce the channel width in the U-Net to 70% of its original size. Table 1 presents the final latency, computational cost, and parameter count of our model in comparison to the original SD-Turbo.

Building on recent progress in one-step diffusion-based generation [49, 50], we introduce adversarial loss during training to improve texture fidelity. In the first stage, the model is trained using a combination of MSE loss, LPIPS [51], and adversarial loss. In the second stage, we incorporate the multi-layer feature distillation loss to retain knowledge from the full-capacity model during pruning.

In the first training phase, we train the unpruned SD U-Net equipped with LiteED for 80,000 steps. In the second phase, we first apply channel pruning over 80,000 steps, followed by module-wise online annealing pruning for an additional 8,000 steps. The total number of annealing steps is set to $T = 8000$. A fixed batch size of 64 is used throughout the entire training process. We employ the AdamW optimizer with a learning rate of 1×10^{-4} , and the timestep is fixed at $t = 999$ for one-step diffusion. Additionally, the original text embedding is replaced with a learnable embedding vector.

4 Experiments

4.1 Experimental Settings

The training dataset comprises approximately 500K high-quality images from LSDIR [52] and 10K images from FFHQ [53]. During training, images are randomly cropped into 512×512 patches. Low-quality counterparts are synthesized using the widely adopted degradation pipeline from Real-ESRGAN [1]. For evaluation, we follow the protocols in [18, 22] and report results on the DRealSR [54] and RealSR [44] benchmarks.

We compare the proposed PocketSR with four state-of-the-art multi-step methods—StableSR [3], DiffBIR [4], SeeSR [16], and ResShift [6]—as well as three leading single-step methods: SinSR [19], AdcSR [18], and OSEDiff [22]. All models are evaluated using a comprehensive set of metrics, including perceptual similarity metrics (LPIPS [51], DISTS [55]), fidelity metrics (PSNR, SSIM [56]), and no-reference quality metrics (NIQE [57], MUSIQ [58]).

4.2 Comparison with State-of-the-Arts

Quantitative and Efficiency Comparison. Table 2 reports quantitative results on RealSR [44] and DRealSR [54], with efficiency metrics listed in the last five rows. The results show that our method achieves strong super-resolution performance with excellent computational efficiency. First, the proposed single-step model, PocketSR, has only 146M parameters, achieves the lowest MACs among all methods, and processes a 512×512 image in 0.016 seconds on a single GPU—nearly

Table 2: Quantitative and efficiency comparisons with state-of-the-art methods on real-world datasets are presented. The best results for each metric are highlighted in bold. PocketSR delivers real-time inference at over 60 FPS on a single GPU with about 19.5 TFLOPS for FP32 for 512×512 inputs, while maintaining competitive quantitative performance.

Datasets	Metrics	StableSR [3]	DiffBIR [4]	SeeSR [16]	ResShift [6]	SinSR [19]	OSDiff [22]	AdcSR [18]	PocketSR
RealSR [44]	LPIPS↓	0.3018	0.3636	0.3009	0.3460	0.3188	0.2921	0.2885	0.2713
	DISTS↓	0.2288	0.2312	0.2223	0.2498	0.2353	0.2128	0.2129	0.2094
	PSNR↑	24.70	24.75	25.18	26.31	26.28	25.15	25.47	25.47
	SSIM↑	0.7085	0.6567	0.7216	0.7421	0.7347	0.7341	0.7301	0.7330
	NIQE↓	5.912	5.535	5.408	7.264	6.287	5.648	5.350	5.067
	MUSIQ↑	65.78	64.98	69.77	58.43	60.80	69.09	69.90	67.07
DRealSR [54]	LPIPS↓	0.3284	0.4557	0.3189	0.4006	0.3665	0.2968	0.3046	0.2962
	DISTS↓	0.2269	0.2748	0.2315	0.2656	0.2485	0.2165	0.2200	0.2139
	PSNR↑	28.03	26.71	28.17	28.46	28.36	27.92	28.10	28.05
	SSIM↑	0.7536	0.6571	0.7691	0.7673	0.7515	0.7835	0.7726	0.7675
	NIQE↓	6.524	6.312	6.397	8.125	6.991	6.490	6.450	5.809
	MUSIQ↑	58.51	61.07	64.93	50.60	55.33	64.65	66.26	63.85
Parameters (M)		1410	1717	2524	119	119	1775	456	146
MACs (G)		79940	24234	65857	5491	2649	2265	496	225
Sampling Steps		200	50	50	15	1	1	1	1
Inference Time (s)		11.5	2.7	4.3	0.71	0.13	0.11	0.03	0.016
FPS		0.09	0.37	0.23	1.4	7.7	9.1	33.3	62.5

twice as fast as AdcSR. This low latency and lightweight design make it ideal for real-time and edge deployment. Second, PocketSR attains the best LPIPS, DISTS, and NIQE scores, demonstrating superior perceptual quality. Notably, on the DRealSR dataset, PocketSR surpasses the second-best method by **10%** in NIQE, indicating clearer texture restoration. Third, it delivers competitive fidelity, achieving PSNR and SSIM on par with AdcSR on RealSR and clearly outperforming multi-step models such as StableSR, DiffBIR, and SeeSR.

Qualitative Comparison. Figure 4 shows qualitative comparisons, demonstrating that our method consistently maintains high fidelity and excels in detail reconstruction. In the first row, only DiffBIR, ResShift, SinSR, and PocketSR successfully recover the diagonal striped texture in the upper-right corner. However, the textures produced by DiffBIR and SinSR appear visually unrealistic. Among single-step methods, only PocketSR reconstructs an accurate and perceptually convincing pattern, highlighting its strength in preserving fine details. The second row further shows that PocketSR is the only method able to restore the building’s structural details, reinforcing its high fidelity and detail recovery capabilities. Figure 1 showcases results across a broader range of natural scenes, including animals and animes. These results further verify that PocketSR not only achieves faithful reconstructions but also delivers rich, fine-grained textures across diverse visual contexts.

4.3 Ablation Study

We carefully analyze the effects of the proposed lite encoder and decoder, online annealing pruning, and multi-layer feature distillation, demonstrating an excellent trade-off between super-resolution quality and efficiency through extensive experiments.

Effect of Adaptive Skip Connection and Dual-path Feature Injection. The proposed lite encoder simplifies the original SD encoder to improve efficiency, which inevitably introduces information loss. To address this, we introduce the Adaptive Skip Connection (ASC), which flexibly transfers essential features to the decoder during encoding. This not only eases the training of the diffusion U-Net but also improves both fidelity and perceptual quality in the super-resolution results. Additionally, we design the Dual-path Feature Injection (DFI) module to alleviate the information bottleneck between the encoder and U-Net (see Sect. 3.1). As shown in Table 3, both ASC and DFI consistently improve performance across nearly all metrics with minimal overhead. Figure 5 further confirms their effectiveness: removing either module causes visible degradation, particularly in the word “Sausage” (first row) and the plastic chair edges (second row).

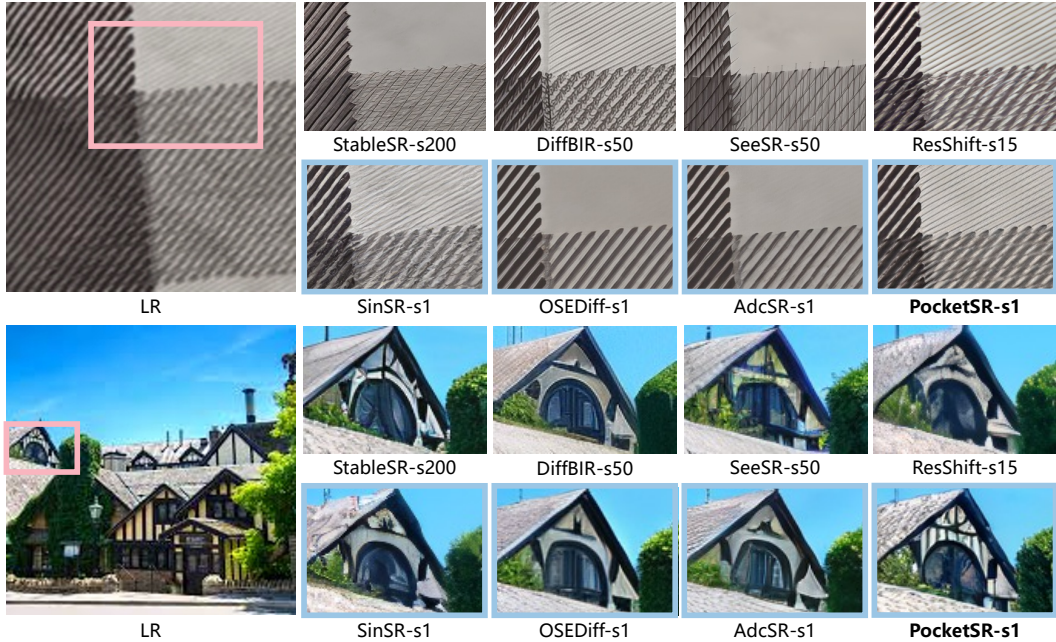


Figure 4: Qualitative results on real-world images. Single-step methods are highlighted for clarity. PocketSR delivers competitive performance, generating well-preserved structures and fine-grained textures, even when compared to multi-step models.

Decoder	Encoder	PSNR \uparrow	SSIM \uparrow	LPIPS \downarrow	DISTS \downarrow	NIQE \downarrow	Time (ms)	MACs (G)	Param. (M)
Lite Dec. (Ours)	Lite Enc. (Ours)	25.61	0.7431	0.2474	0.1911	5.200	31.4	481.6	868.3
	Lite Enc. w/o ASC	25.42	0.7426	0.2737	0.2050	5.329	30.7	480.8	868.3
	Lite Enc. w/o DFI	25.35	0.7427	0.2580	0.1940	5.136	31.1	478.6	867.6
	PixelUnshuffle	25.23	0.7417	0.2697	0.2028	5.552	30.5	474.8	867.7
	SD Enc.	25.19	0.7259	0.2685	0.1981	5.092	51.7	1032.2	901.4
SD Dec.	Lite Enc. (Ours)	25.95	0.7503	0.2390	0.1843	6.899	58.1	1669.7	916.2
	SD Enc.	26.00	0.7548	0.2445	0.1892	6.898	79.7	2221.2	949.6

Table 3: We conducted ablation studies on the core architectural components of LiteED, including the Adaptive Skip Connection (ASC) and Dual-path Feature Injection (DFI). Additionally, we compared the proposed lightweight encoder with alternative designs to validate the effectiveness of our architecture. Finally, we replaced the decoder to assess the structural robustness of LiteED.

Comparison between the Lite Encoder and Alternative Encoding Strategies. We compare our lite encoder with the PixelUnshuffle approach and the original SD encoder (SD Enc.). PixelUnshuffle, introduced by AdcSR [18], is a lightweight method for injecting low-resolution (LR) features. Despite similar computational cost, our encoder consistently outperforms PixelUnshuffle across all metrics, with up to **8.3%** improvement in LPIPS. Moreover, our design achieves superior performance on reference-based metrics than the SD encoder, with only **46.7%** of its computational cost. We attribute this to the absence of skip connections and the potential bottleneck in the SD encoder, which may result in the loss of fidelity-critical information. As shown in Figure 5, PixelUnshuffle often causes fine detail loss (first row) and oversmoothing (second row), while the SD encoder tends to produce unnatural textures. These results highlight that a well-designed lightweight encoder can outperform complex counterparts in SR tasks, offering valuable insights for efficient model design.

Compatibility with more powerful image decoders. Prior studies [59, 18] have shown that decoder complexity often has a greater impact on performance than encoder complexity. Building on this, we investigate the decoder flexibility of LiteED by replacing its decoder with the original SD decoder, while keeping the lite encoder (w/ ASC & DFI) unchanged. This substitution leads to improved SR quality, albeit with a **247%** increase in computational overhead. These results underscore the generalizability of LiteED, enabling flexible decoder adjustment to balance efficiency

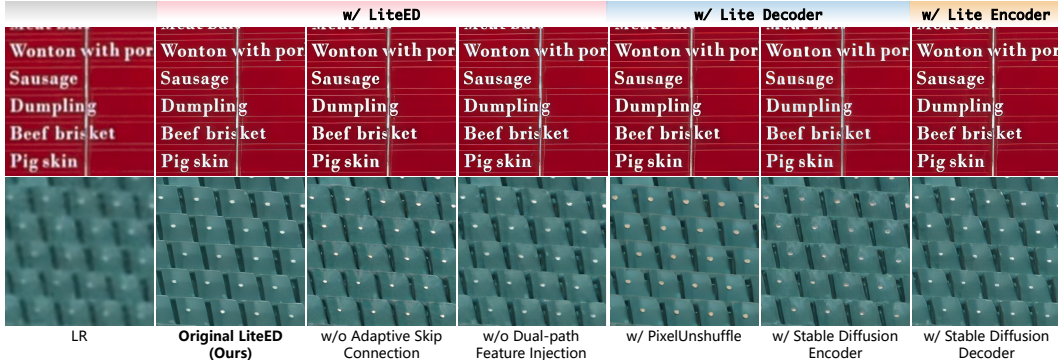


Figure 5: Ablation study of the LiteED design on “Canon 003” from RealSR (top) and “DSC 1286” from DRealSR (bottom).



Figure 6: Ablation study of our pruning strategy on “Nikon 004” and “Nikon 015” images from RealSR.

Table 4: Ablation study on pruning strategies. We conduct ablation studies on the online annealing strategy and the multi-layer feature distillation loss employed during pruning. Additionally, we compare the effectiveness of multi-layer distillation against single-layer distillation applied solely to the output layer of the U-Net.

Strategy	Online Annealing	Multi-layer Distillation	LPIPS↓	DISTS↓	NIQE↓
Ours	✓	✓	0.2713	0.2094	5.067
(1)	✗	✓	0.2732	0.2120	5.126
(2)	✓	✗	0.2816	0.2162	5.097
(3)	✓	Single-layer	0.2762	0.2116	5.077

and performance. We also compare our design with the original SD VAE (w/o ASC & DFI). The variant using the SD decoder and lite encoder achieves comparable performance with a **24.8%** reduction in computational cost, further validating the effectiveness of the LiteED architecture.

Effect of Online Annealing Pruning. In Table 4, we compare the proposed online annealing pruning strategy with direct lightweight module replacement, denoted as Strategy (1). Our approach consistently outperforms the baseline across all metrics, especially the no-reference NIQE score, thanks to its progressive knowledge transfer that better preserves the SD model’s generative prior. As shown in Figure 6, while direct pruning fails to recover clear brick patterns and wheat textures, our method yields visually superior and high-quality results.

Effect of Multi-layer Feature Distillation. Multi-layer feature distillation is introduced to enhance the stability and robustness of knowledge transfer during pruning. As shown in Table 4, removing it (Strategy 2) degrades performance across all metrics, with LPIPS showing the largest drop (**3.8%**). We also evaluate single-layer distillation at the U-Net output (Strategy 3), which slightly outperforms Strategy 2 but still lags behind the full multi-layer setup. As illustrated in Figure 6, removing multi-layer distillation results in noticeable noise and artifacts due to unstable training dynamics.

5 Conclusion and limitation

We present PocketSR, a highly efficient single-step model for real-world image super-resolution. By replacing the heavy VAE in SD with LiteED, PocketSR reduces parameters and latency while preserving fidelity. Our proposed pruning strategy further enhances efficiency by progressively transferring generative priors to lightweight modules, optimizing performance without compromising quality. Experiments show that it achieves significant speedup and performance comparable to state-of-the-art RealSR models, making it practical for broad deployment.

One limitation of PocketSR is that its detail generation capability under severe degradations remains to be improved. Moreover, the current framework has not yet been optimized in conjunction with edge hardware, which we identify as a promising avenue for future research.

A Supplementary Materials

In the supplementary materials, we provide the following materials:

1. Ablation experiments on pruning locations.
2. The effectiveness of combining channel pruning with multi-layer feature distillation and the selection of pruning ratios.
3. Performance on the DIV2K validation set [3].
4. The effectiveness of Stable Diffusion prior.
5. Details of the lite decoder structure.
6. Details of our training loss.
7. More qualitative comparisons.

A.1 Ablation Experiments on Pruning Locations

As discussed in Section 3.2.2, the choice of pruning location plays a critical role in model performance. In particular, pruning shallower modules has a greater impact on super-resolution quality, whereas deeper blocks can be pruned with relatively minor performance degradation. We conduct ablation studies on four computationally intensive components within the diffusion U-Net: residual blocks, cross-attention layers, self-attention layers, and feed-forward networks (FFNs). U-Net depth levels are categorized as I, II, III, IV, from shallowest to deepest. All experiments are performed on the RealSR dataset [44].

Table 5: Comparison of quantitative performance and efficiency across residual block pruning locations. Our selected setting is marked in **bold**.

Pruning Position	PSNR \uparrow	SSIM \uparrow	LPIPS \downarrow	DISTS \downarrow	FID \downarrow	Time (ms)	MACs (G)	Param. (M)
None	24.84	0.7232	0.2653	0.2015	110.46	17.73	279	430
Depth IV	25.08	0.7307	0.2673	0.2047	116.76	17.32	278	422
Depth III, IV (Ours)	24.98	0.7294	0.2695	0.2041	117.76	15.79	268	382
Depth II, III, IV	24.51	0.7060	0.2866	0.2162	133.09	14.16	258	372
Depth I, II, III, IV	24.25	0.6929	0.3019	0.2253	131.81	12.59	250	370

Table 6: Comparison of quantitative performance and efficiency across cross-attention layer pruning locations. Our selected setting is marked in **bold**.

Pruning Position	PSNR \uparrow	SSIM \uparrow	LPIPS \downarrow	DISTS \downarrow	FID \downarrow	Time (ms)	MACs (G)	Param. (M)
None	24.84	0.7232	0.2653	0.2015	110.46	17.73	279	430
Depth IV	25.14	0.7313	0.2676	0.2052	116.21	17.33	278	427
Depth III, IV	24.92	0.7270	0.2671	0.2032	112.89	16.71	276	410
Depth II, III, IV	24.76	0.7224	0.2682	0.2026	111.07	15.91	273	404
Depth I, II, III, IV (Ours)	24.97	0.7307	0.2666	0.2031	112.85	14.97	271	401

As shown in Table 5, pruning residual blocks at shallow depths (I and II) results in significant degradation in perceptual metrics such as LPIPS, DISTS, and FID. Consequently, we limit pruning to deeper layers (depths III and IV). The ablation study on cross-attention layers, presented in Table 6, reveals that their contribution is limited, as super-resolution primarily depends on fine-grained visual details rather than high-level semantic alignment. We find that pruning all cross-attention layers has minimal impact on overall model quality.

Table 7 reports the ablation results for self-attention layer pruning. Pruning at depths III and above leads to a noticeable decline in perceptual metrics. While PSNR and SSIM slightly improve when pruning layers at depths III and IV, we attribute this to oversmoothing effects rather than actual perceptual gains. Lastly, we examine the pruning positions of feed-forward networks (Table 8). Balancing performance and efficiency, we opt to prune FFNs at depths III and IV.

Table 7: Comparison of quantitative performance and efficiency across self-attention layer pruning locations. Our selected setting is marked in **bold**.

Pruning Position	PSNR \uparrow	SSIM \uparrow	LPIPS \downarrow	DISTS \downarrow	FID \downarrow	Time (ms)	MACs (G)	Param. (M)
None	24.84	0.7232	0.2653	0.2015	110.46	17.73	279	430
Depth IV (Ours)	25.14	0.7315	0.2677	0.2056	116.56	17.49	279	430
Depth III, IV	25.43	0.7308	0.2757	0.2257	147.15	17.08	278	430
Depth II, III, IV	23.51	0.6428	0.3583	0.2640	196.66	16.54	274	430
Depth I, II, III, IV	22.50	0.5310	0.4611	0.3038	244.87	13.18	242	430

Table 8: Comparison of quantitative performance and efficiency across feed-forward network pruning locations. Our selected setting is marked in **bold**.

Pruning Position	PSNR \uparrow	SSIM \uparrow	LPIPS \downarrow	DISTS \downarrow	FID \downarrow	Time (ms)	MACs (G)	Param. (M)
None	24.84	0.7232	0.2653	0.2015	110.46	17.73	279	430
Depth IV	25.08	0.7307	0.2673	0.2047	116.76	17.32	278	422
Depth III, IV (Ours)	24.98	0.7294	0.2695	0.2041	117.76	15.79	268	382
Depth II, III, IV	24.51	0.7060	0.2866	0.2162	133.09	14.16	258	372
Depth I, II, III, IV	24.25	0.6929	0.3019	0.2253	131.81	12.59	250	370

A.2 Channel Pruning with Multi-layer Feature Distillation

Table 9 presents the impact of the proposed multi-layer feature distillation on channel pruning, alongside performance and efficiency comparisons across varying pruning ratios. As the pruning ratio increases, model efficiency improves, but perceptual quality gradually declines. Figure 7 further illustrates that pruning without multi-layer feature distillation leads to a significant performance drop, whereas incorporating it effectively mitigates this degradation by preserving prior knowledge that would otherwise be lost. Balancing performance and efficiency, we adopt 30% channel pruning with multi-layer feature distillation as our final configuration.

Table 9: Comparison of performance and efficiency of channel pruning at different ratios with and without multi-layer feature distillation. The selected setting is highlighted in **bold**.

Pruning Ratio	w/ Multi-layer Distillation			w/o Multi-layer Distillation			Time (ms)	MACs (G)	Param. (M)
	LPIPS \downarrow	DISTS \downarrow	FID \downarrow	LPIPS \downarrow	DISTS \downarrow	FID \downarrow			
0%	0.2474	0.1911	101.82	0.2474	0.1911	101.82	31.37	482	868
10%	0.2625	0.1983	103.80	0.2669	0.2048	106.95	25.78	399	704
20%	0.2647	0.1981	107.11	0.2618	0.1983	115.21	22.19	347	561
30%	0.2653	0.2015	110.46	0.2653	0.2057	126.47	17.73	279	430
40%	0.2712	0.2058	116.51	0.2798	0.2148	140.85	15.25	239	320
50%	0.2865	0.2126	126.53	0.3090	0.2290	156.72	11.24	186	224

A.3 Performance on the DIV2K Validation Set

To further assess the robustness of our method under more diverse degradations, we evaluate it on the DIV2K validation set, with results presented in Table 10. This dataset, introduced by StableSR [3], contains low-resolution images generated using Real-ESRGAN [1]. PocketSR surpasses previous single-step and even multi-step methods in LPIPS and DISTS, ranks second in FID and NIQE, and performs comparably to other single-step approaches on the remaining metrics. These results highlight PocketSR’s strong perceptual quality and its robustness to challenging degradations.

A.4 Effect of Stable Diffusion Prior

PocketSR is built on a pre-trained Stable Diffusion (SD) model, followed by pruning and distillation. To assess whether PocketSR successfully preserves the prior knowledge from the pre-trained SD,

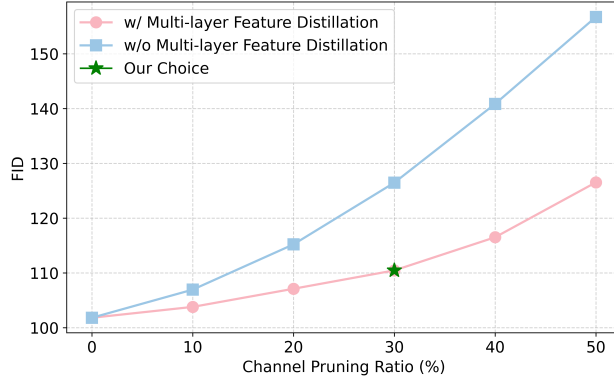


Figure 7: FID comparison of channel pruning at different ratios with and without Multi-layer Feature Distillation.

Table 10: Quantitative comparisons with state-of-the-art methods on the DIV2K validation set. The best results for each metric are highlighted in **bold**, and the second-best are underlined.

Datasets	Metrics	StableSR [3]	DiffBIR [4]	SeeSR [16]	ResShift [6]	SinSR [19]	OSDiff [22]	AdcSR [18]	PocketSR
DIV2K Val. [3]	LPIPS↓	0.3113	0.3524	0.3194	0.3349	0.3240	0.2941	0.2853	0.2801
	DISTS↓	0.2048	0.2128	0.1968	0.2213	0.2066	0.1976	0.1899	0.1830
	PSNR↑	23.26	23.64	23.68	24.65	24.41	23.72	23.74	23.85
	SSIM↑	0.5726	0.5647	0.6043	0.6181	0.6018	0.6108	0.6017	0.6015
	FID↓	24.44	30.72	25.90	36.11	35.57	26.32	25.52	25.25
	NIQE↓	4.760	4.700	4.810	6.820	6.020	4.710	4.360	4.415
	MUSIQ↑	65.92	65.81	68.67	61.09	62.82	67.97	68.00	66.38

we conduct an ablation study on the SD prior, as shown in Table 11. Specifically, we retain the pruned architecture of PocketSR but remove the SD-based initialization for the U-Net, training the entire model from scratch instead. This variant is referred to as “w/o SD prior”. Results show that leveraging the SD prior yields superior performance across all metrics except NIQE, with a notable PSNR improvement of nearly 0.8 dB. The higher NIQE score is likely due to GAN-induced artifacts arising from the lack of SD prior guidance.

Table 11: Ablation Study of Stable Diffusion prior on the RealSR and DRealSR datasets. The best results for each metric are highlighted in **bold**.

Datasets	Methods	PSNR↑	SSIM↑	LPIPS↓	DISTS↓	NIQE↓	MUSIQ↑
RealSR	Ours	25.47	0.7330	0.2713	0.2094	5.067	67.07
	w/o SD Prior	24.66	0.7080	0.2718	0.2132	4.912	65.72
DRealSR	Ours	28.05	0.7675	0.2962	0.2139	5.809	63.85
	w/o SD Prior	27.22	0.7364	0.3034	0.2181	5.697	62.32

A.5 Details of the Lite Decoder Structure

This section describes the architecture of the proposed Lite Decoder. In latent diffusion models, VAEs are typically employed to map images from pixel space to latent space, with reconstruction quality closely tied to the decoder’s design. To maintain model efficiency, we introduce structural simplification and channel pruning, aiming to balance lightweight design with high-fidelity reconstruction.

As illustrated in Figure 8, we simplify the original Stable Diffusion (SD) VAE decoder, which consists of five sequential modules—each typically composed of three ResBlocks, self-attention layers, and upsampling operations. Since the decoder performs 8× spatial upsampling, all upsampling modules are retained. However, we remove the attention-equipped modules due to their high quadratic computational cost. To preserve reconstruction quality, a single ResBlock is placed after the final upsampling stage as the output head. Furthermore, we reduce the number of channels across the entire decoder, capping each layer at 64 channels.

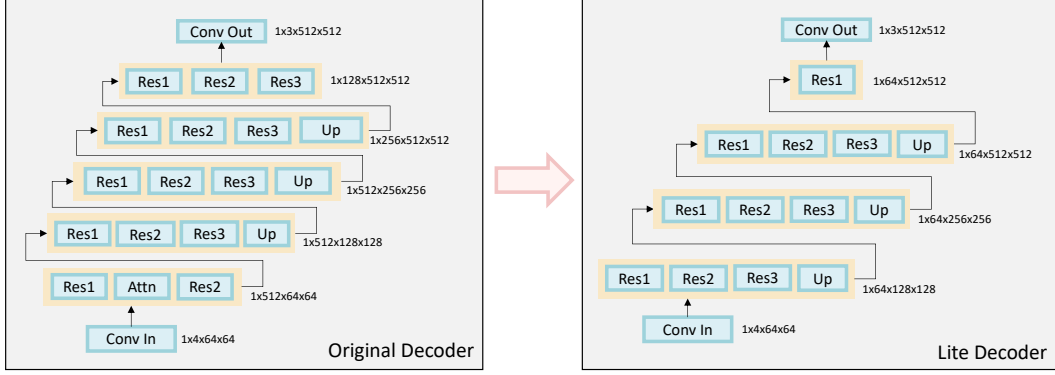


Figure 8: Structural comparison between the original SD VAE decoder and our Lite Decoder.

A.6 Details of Our Training Loss

Figure 9 illustrates the training pipeline of our model, along with the loss functions employed at each stage. The training process consists of two stages. In the first stage, we train the entire model end-to-end by replacing the original encoder–decoder with LiteED while keeping the U-Net intact. The loss used in this stage is a weighted sum of MSE, LPIPS, and adversarial losses:

$$\mathcal{L}_{\text{total}} = \lambda_1 \mathcal{L}_{\text{mse}} + \lambda_2 \mathcal{L}_{\text{lpips}} + \lambda_3 \mathcal{L}_{\text{gan}}, \quad (3)$$

where $\lambda_1 = 2$, $\lambda_2 = 2$, and $\lambda_3 = 0.25$.

In the second stage, LiteED is frozen, and we fine-tune the pruned U-Net. The fully trained U-Net from the first stage serves as the teacher, and multi-layer feature distillation is used to guide the pruned model. The original losses from the first stage are retained, with an additional distillation loss incorporated:

$$\mathcal{L}_{\text{total}} = \lambda_1 \mathcal{L}_{\text{mse}} + \lambda_2 \mathcal{L}_{\text{lpips}} + \lambda_3 \mathcal{L}_{\text{gan}} + \lambda_4 \mathcal{L}_{\text{distill}}, \quad (4)$$

where $\lambda_1 = 2$, $\lambda_2 = 2$, $\lambda_3 = 0.25$, and $\lambda_4 = 0.001$.

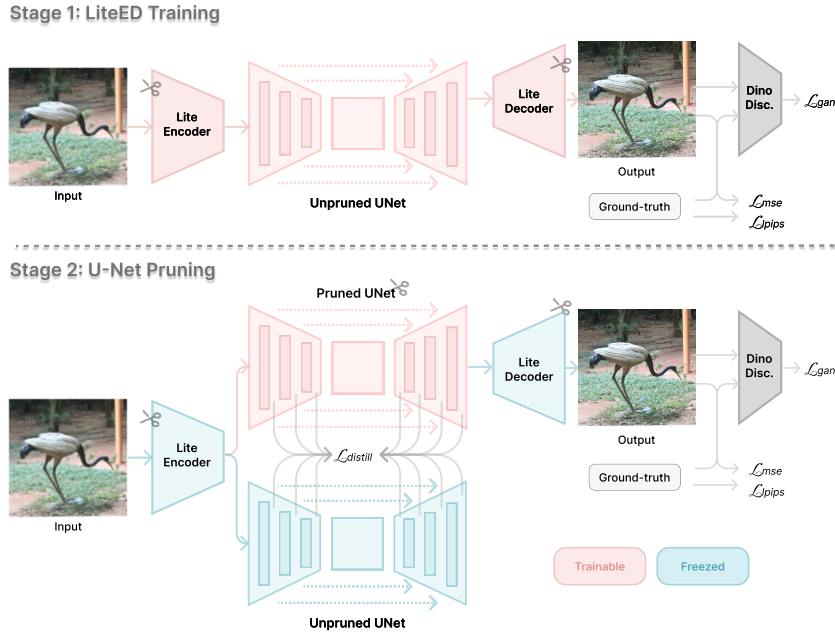


Figure 9: Loss composition at different training stages.

A.7 More Qualitative Comparisons

Figures 10 and 11 provide additional qualitative comparisons. As shown in Figure 10, PocketSR exhibits clear advantages in fidelity, particularly in recovering architectural details and regular structures. In contrast, other methods—especially multi-step approaches—often hallucinate content and diverge from the ground truth, despite their strong generative capabilities. Beyond its high fidelity, PocketSR also excels at fine texture generation, as illustrated in Figure 11, where it reconstructs high-quality textures for challenging elements such as starry skies, petals, wood, and rocks.

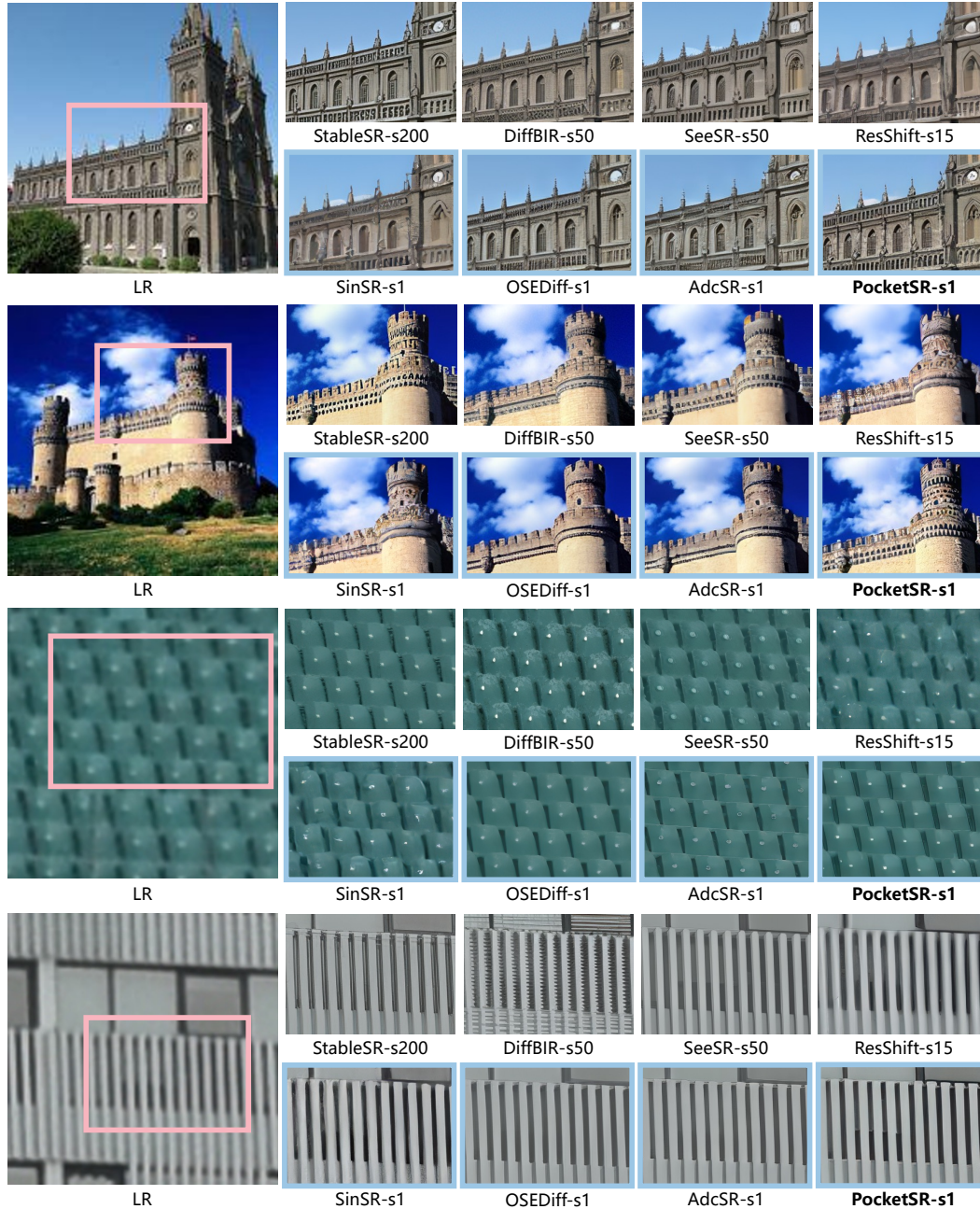


Figure 10: More qualitative results on real-world images. Single-step methods are highlighted for clarity. (1/2)

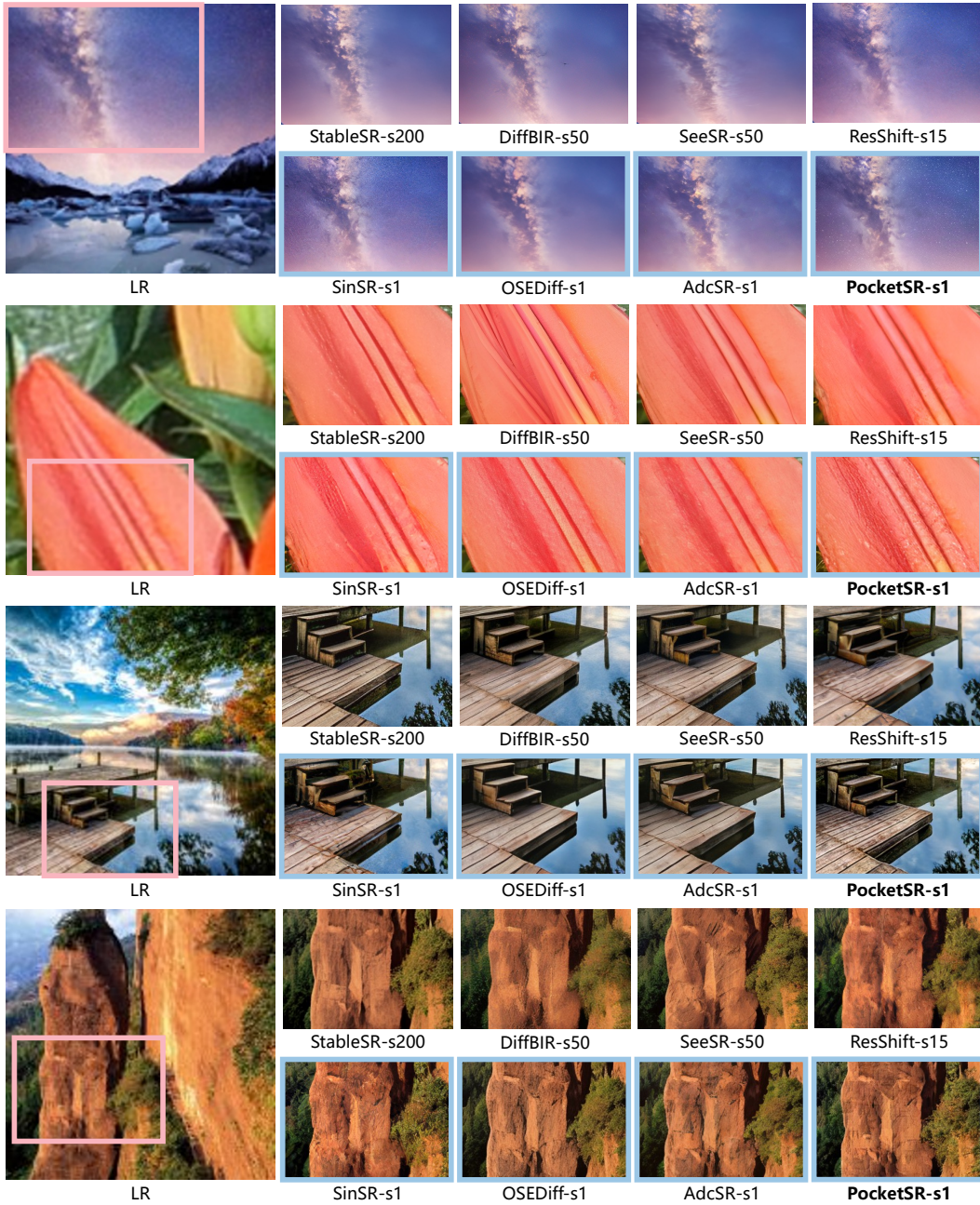


Figure 11: More qualitative results on real-world images. Single-step methods are highlighted for clarity. (2/2)

References

- [1] X. Wang, L. Xie, C. Dong, and Y. Shan, “Real-esrgan: Training real-world blind super-resolution with pure synthetic data,” in *ICCV*, 2021, pp. 1905–1914.
- [2] K. Zhang, J. Liang, L. Van Gool, and R. Timofte, “Designing a practical degradation model for deep blind image super-resolution,” in *ICCV*, 2021, pp. 4791–4800.
- [3] J. Wang, Z. Yue, S. Zhou, K. C. Chan, and C. C. Loy, “Exploiting diffusion prior for real-world image super-resolution,” *IJCV*, 2024.
- [4] X. Lin, J. He, Z. Chen, Z. Lyu, B. Dai, F. Yu, Y. Qiao, W. Ouyang, and C. Dong, “Diffbir: Toward blind image restoration with generative diffusion prior,” in *ECCV*. Springer, 2024, pp. 430–448.
- [5] T. Yang, R. Wu, P. Ren, X. Xie, and L. Zhang, “Pixel-aware stable diffusion for realistic image super-resolution and personalized stylization,” in *ECCV*. Springer, 2024, pp. 74–91.
- [6] Z. Yue, J. Wang, and C. C. Loy, “Resshift: Efficient diffusion model for image super-resolution by residual shifting,” *NeurIPS*, vol. 36, pp. 13 294–13 307, 2023.
- [7] J. Ho, A. Jain, and P. Abbeel, “Denoising diffusion probabilistic models,” *NeurIPS*, vol. 33, pp. 6840–6851, 2020.
- [8] J. Song, C. Meng, and S. Ermon, “Denoising diffusion implicit models,” *arXiv preprint arXiv:2010.02502*, 2020.
- [9] R. Rombach, A. Blattmann, D. Lorenz, P. Esser, and B. Ommer, “High-resolution image synthesis with latent diffusion models,” in *CVPR*, 2022, pp. 10 684–10 695.
- [10] C. Saharia, W. Chan, S. Saxena, L. Li, J. Whang, E. L. Denton, K. Ghasemipour, R. Gontijo Lopes, B. Karagol Ayan, T. Salimans *et al.*, “Photorealistic text-to-image diffusion models with deep language understanding,” *NeurIPS*, vol. 35, pp. 36 479–36 494, 2022.
- [11] J. Chen, J. Yu, C. Ge, L. Yao, E. Xie, Y. Wu, Z. Wang, J. Kwok, P. Luo, H. Lu *et al.*, “Pixart- α : Fast training of diffusion transformer for photorealistic text-to-image synthesis,” *arXiv preprint arXiv:2310.00426*, 2023.
- [12] P. Esser, S. Kulal, A. Blattmann, R. Entezari, J. Müller, H. Saini, Y. Levi, D. Lorenz, A. Sauer, F. Boesel *et al.*, “Scaling rectified flow transformers for high-resolution image synthesis,” in *ICML*, 2024.
- [13] B. F. Labs, “Flux,” <https://github.com/black-forest-labs/flux>, 2024.
- [14] J. Li, J. Cao, Y. Guo, W. Li, and Y. Zhang, “One diffusion step to real-world super-resolution via flow trajectory distillation,” *arXiv preprint arXiv:2502.01993*, 2025.
- [15] F. Yu, J. Gu, Z. Li, J. Hu, X. Kong, X. Wang, J. He, Y. Qiao, and C. Dong, “Scaling up to excellence: Practicing model scaling for photo-realistic image restoration in the wild,” in *CVPR*, 2024, pp. 25 669–25 680.
- [16] R. Wu, T. Yang, L. Sun, Z. Zhang, S. Li, and L. Zhang, “Seesr: Towards semantics-aware real-world image super-resolution,” in *CVPR*, 2024, pp. 25 456–25 467.
- [17] H. Sun, W. Li, J. Liu, K. Zhou, Y. Chen, Y. Guo, Y. Li, R. Pei, L. Peng, and Y. Yang, “Beyond pixels: Text enhances generalization in real-world image restoration,” *arXiv preprint arXiv:2412.00878*, 2024.
- [18] B. Chen, G. Li, R. Wu, X. Zhang, J. Chen, J. Zhang, and L. Zhang, “Adversarial diffusion compression for real-world image super-resolution,” in *CVPR*, 2025.
- [19] Y. Wang, W. Yang, X. Chen, Y. Wang, L. Guo, L.-P. Chau, Z. Liu, Y. Qiao, A. C. Kot, and B. Wen, “Sinsr: diffusion-based image super-resolution in a single step,” in *CVPR*, 2024.
- [20] R. Xie, C. Zhao, K. Zhang, Z. Zhang, J. Zhou, J. Yang, and Y. Tai, “Addsr: Accelerating diffusion-based blind super-resolution with adversarial diffusion distillation,” *arXiv preprint arXiv:2404.01717*, 2024.
- [21] L. Dong, Q. Fan, Y. Guo, Z. Wang, Q. Zhang, J. Chen, Y. Luo, and C. Zou, “Tsd-sr: One-step diffusion with target score distillation for real-world image super-resolution,” *arXiv preprint arXiv:2411.18263*, 2024.
- [22] R. Wu, L. Sun, Z. Ma, and L. Zhang, “One-step effective diffusion network for real-world image super-resolution,” *NeurIPS*, vol. 37, pp. 92 529–92 553, 2025.

- [23] A. Zhang, Z. Yue, R. Pei, W. Ren, and X. Cao, “Degradation-guided one-step image super-resolution with diffusion priors,” *arXiv preprint arXiv:2409.17058*, 2024.
- [24] D. Hu, J. Chen, X. Huang, H. Coskun, A. Sahni, A. Gupta, A. Goyal, D. Lahiri, R. Singh, Y. Idelbayev *et al.*, “Snapgen: Taming high-resolution text-to-image models for mobile devices with efficient architectures and training,” *arXiv preprint arXiv:2412.09619*, 2024.
- [25] B. Lim, S. Son, H. Kim, S. Nah, and K. Mu Lee, “Enhanced deep residual networks for single image super-resolution,” in *CVPRW*, 2017, pp. 136–144.
- [26] Y. Zhang, K. Li, K. Li, L. Wang, B. Zhong, and Y. Fu, “Image super-resolution using very deep residual channel attention networks,” in *ECCV*, 2018, pp. 286–301.
- [27] J. Liang, J. Cao, G. Sun, K. Zhang, L. Van Gool, and R. Timofte, “Swinir: Image restoration using swin transformer,” in *ICCV*, 2021, pp. 1833–1844.
- [28] S. W. Zamir, A. Arora, S. Khan, M. Hayat, F. S. Khan, and M.-H. Yang, “Restormer: Efficient transformer for high-resolution image restoration,” in *CVPR*, 2022, pp. 5728–5739.
- [29] C. Ledig, L. Theis, F. Huszár, J. Caballero, A. Cunningham, A. Acosta, A. Aitken, A. Tejani, J. Totz, Z. Wang *et al.*, “Photo-realistic single image super-resolution using a generative adversarial network,” in *CVPR*, 2017, pp. 4681–4690.
- [30] X. Wang, Y. Li, H. Zhang, and Y. Shan, “Towards real-world blind face restoration with generative facial prior,” in *CVPR*, 2021, pp. 9168–9178.
- [31] T. Yang, P. Ren, X. Xie, and L. Zhang, “Gan prior embedded network for blind face restoration in the wild,” in *CVPR*, 2021, pp. 672–681.
- [32] L. Yang, S. Wang, S. Ma, W. Gao, C. Liu, P. Wang, and P. Ren, “Hifacegan: Face renovation via collaborative suppression and replenishment,” in *ACMMM*, 2020, pp. 1551–1560.
- [33] J. Liang, H. Zeng, and L. Zhang, “Details or artifacts: A locally discriminative learning approach to realistic image super-resolution,” in *CVPR*, 2022, pp. 5657–5666.
- [34] L. Xie, X. Wang, X. Chen, G. Li, Y. Shan, J. Zhou, and C. Dong, “Desra: Detect and delete the artifacts of gan-based real-world super-resolution models,” in *ICML*, ser. Proceedings of Machine Learning Research, vol. 202. PMLR, 2023, pp. 38 204–38 226.
- [35] H. Sun, W. Li, J. Liu, H. Chen, R. Pei, X. Zou, Y. Yan, and Y. Yang, “Coser: Bridging image and language for cognitive super-resolution,” in *CVPR*, 2024, pp. 25 868–25 878.
- [36] Z. Wang, C. Lu, Y. Wang, F. Bao, C. Li, H. Su, and J. Zhu, “Prolificdreamer: High-fidelity and diverse text-to-3d generation with variational score distillation,” *NeurIPS*, vol. 36, pp. 8406–8441, 2023.
- [37] T. Castells, H.-K. Song, T. Piao, S. Choi, B.-K. Kim, H. Yim, C. Lee, J. G. Kim, and T.-H. Kim, “Edgefusion: on-device text-to-image generation,” *arXiv preprint arXiv:2404.11925*, 2024.
- [38] G. Fang, X. Ma, and X. Wang, “Structural pruning for diffusion models,” in *NeurIPS*, 2023.
- [39] Y. Zhu, X. Liu, and Q. Liu, “Slimflow: Training smaller one-step diffusion models with rectified flow,” in *ECCV*. Springer, 2024, pp. 342–359.
- [40] Y. Zhao, Y. Xu, Z. Xiao, H. Jia, and T. Hou, “Mobilediffusion: Instant text-to-image generation on mobile devices,” in *ECCV*. Springer, 2024, pp. 225–242.
- [41] B.-K. Kim, H.-K. Song, T. Castells, and S. Choi, “Bk-sdm: A lightweight, fast, and cheap version of stable diffusion,” in *ECCV*. Springer, 2024, pp. 381–399.
- [42] Y. Li, H. Wang, Q. Jin, J. Hu, P. Chemerys, Y. Fu, Y. Wang, S. Tulyakov, and J. Ren, “Snapfusion: Text-to-image diffusion model on mobile devices within two seconds,” *NeurIPS*, vol. 36, pp. 20 662–20 678, 2023.
- [43] B. Peng, J. Wang, Y. Zhang, W. Li, M.-C. Yang, and J. Jia, “Controlnext: Powerful and efficient control for image and video generation,” *arXiv preprint arXiv:2408.06070*, 2024.
- [44] J. Cai, H. Zeng, H. Yong, Z. Cao, and L. Zhang, “Toward real-world single image super-resolution: A new benchmark and a new model,” in *ICCV*, 2019, pp. 3086–3095.

- [45] R. Zhang, P. Isola, A. A. Efros, E. Shechtman, and O. Wang, “The unreasonable effectiveness of deep features as a perceptual metric,” in *CVPR*, 2018, pp. 586–595.
- [46] A. G. Howard, M. Zhu, B. Chen, D. Kalenichenko, W. Wang, T. Weyand, M. Andreetto, and H. Adam, “Mobilenets: Efficient convolutional neural networks for mobile vision applications,” *arXiv preprint arXiv:1704.04861*, 2017.
- [47] X. Ma, G. Fang, and X. Wang, “Deepcache: Accelerating diffusion models for free,” in *CVPR*, 2024, pp. 15 762–15 772.
- [48] C. Si, Z. Huang, Y. Jiang, and Z. Liu, “Freeu: Free lunch in diffusion u-net,” in *CVPR*, 2024, pp. 4733–4743.
- [49] A. Sauer, D. Lorenz, A. Blattmann, and R. Rombach, “Adversarial diffusion distillation,” in *ECCV*. Springer, 2024, pp. 87–103.
- [50] T. Yin, M. Gharbi, T. Park, R. Zhang, E. Shechtman, F. Durand, and W. T. Freeman, “Improved distribution matching distillation for fast image synthesis,” in *NeurIPS*, 2024.
- [51] R. Zhang, P. Isola, A. A. Efros, E. Shechtman, and O. Wang, “The unreasonable effectiveness of deep features as a perceptual metric,” in *CVPR*, 2018, pp. 586–595.
- [52] Y. Li, K. Zhang, J. Liang, J. Cao, C. Liu, R. Gong, Y. Zhang, H. Tang, Y. Liu, D. Demandolx *et al.*, “Lsdir: A large scale dataset for image restoration,” in *CVPR*, 2023, pp. 1775–1787.
- [53] T. Karras, S. Laine, and T. Aila, “A style-based generator architecture for generative adversarial networks,” in *CVPR*, 2019, pp. 4401–4410.
- [54] P. Wei, Z. Xie, H. Lu, Z. Zhan, Q. Ye, W. Zuo, and L. Lin, “Component divide-and-conquer for real-world image super-resolution,” in *ECCV*. Springer, 2020, pp. 101–117.
- [55] K. Ding, K. Ma, S. Wang, and E. P. Simoncelli, “Image quality assessment: Unifying structure and texture similarity,” *TPAMI*, vol. 44, no. 5, pp. 2567–2581, 2020.
- [56] Z. Wang, A. C. Bovik, H. R. Sheikh, and E. P. Simoncelli, “Image quality assessment: from error visibility to structural similarity,” *TIP*, vol. 13, no. 4, pp. 600–612, 2004.
- [57] A. Mittal, R. Soundararajan, and A. C. Bovik, “Making a “completely blind” image quality analyzer,” *IEEE Signal processing letters*, vol. 20, no. 3, pp. 209–212, 2012.
- [58] J. Ke, Q. Wang, Y. Wang, P. Milanfar, and F. Yang, “Musiq: Multi-scale image quality transformer,” in *ICCV*, 2021, pp. 5148–5157.
- [59] T. Hu, F. Chen, H. Wang, J. Li, W. Wang, J. Sun, and Z. Li, “Complexity matters: Rethinking the latent space for generative modeling,” *Advances in Neural Information Processing Systems*, vol. 36, pp. 29 558–29 579, 2023.